ACS OMEGA

http://pubs.acs.org/journal/acsodf

Article

Controllable Synthesis of a Porous PEI-Functionalized Co_3O_4/rGO Nanocomposite as an Electrochemical Sensor for Simultaneous as Well as Individual Detection of Heavy Metal Ions

Afrasiab Ur Rehman,* Muhammad Fayaz, He Lv, Yang Liu, Jiawei Zhang, Yang Wang, Lijuan Du, Ruihong Wang, and Keying Shi

Cite This: *ACS Omega* 2022, 7, 5870−5882

Read Online

ACCESS | Metrics & More | Article Recommendations | Supporting Information

ABSTRACT: The present study focuses on the strategy of employing an electrochemical sensor with a porous polyethylenimine (PEI)-functionalized Co_3O_4/reduced graphene oxide (rGO) nanocomposite (NCP) to detect heavy metal ions (HMIs: Cd^{2+}, Pb^{2+}, Cu^{2+}, and Hg^{2+}). The porous PEI-functionalized Co_3O_4/rGO NCP (rGO·Co_3O_4·PEI) was prepared via a hydrothermal method. The synthesized NCP was based on a conducting polymer PEI, rGO, nanoribbons of Co_3O_4, and highly dispersed Co_3O_4 nanoparticles (NPs), which have shown excellent performance in the detection of HMIs. The as-prepared PEI-functionalized rGO·Co_3O_4·PEI NCP-modified electrode was used for the sensing/detection of HMIs by means of both square wave anodic stripping voltammetry (SWV) and differential normal pulse voltammetry (DNPV) methods for the first time. Both methods were employed for the simultaneous detection of HMIs, whereas SWV was employed for the individual analysis as well. The limits of detection (LOD; 3σ method) for Cd^{2+}, Pb^{2+}, Cu^{2+}, and Hg^{2+} determined using the rGO·Co_3O_4·PEI NCP−modified electrode were 0.285, 1.132, 1.194, and 1.293 nM for SWV, respectively. Similarly, LODs of Cd^{2+}, Pb^{2+}, Cu^{2+}, and Hg^{2+} were 1.069, 0.285, 2.398, and 1.115 nM, respectively, by DNPV during simultaneous analysis, whereas they were 0.484, 0.878, 0.462, and 0.477 nM, respectively, by SWV in individual analysis.

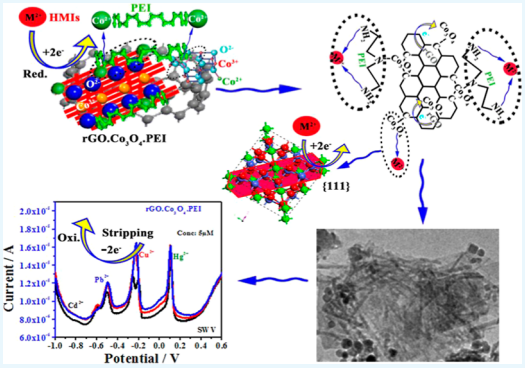

1. INTRODUCTION

Over the past several decades, heavy metal ions (HMIs) have been attracting great attention as they are extremely injurious to the biosphere, and even their minute aggregates are of much threat to human health.[1−3] In order to prevent this, the most sensitive and rapid removal method of trace HMIs is the need of today. Until now, technologically advanced approaches such as electrochemical exploration, anodic stripping voltammetry (ASV), and differential pulse ASV (DPASV) methods have been employed due to their fast response, convenience, and low cost.[4−6]

So far, a stronger electrochemical sensing interaction in an aqueous solution for Pb^{2+} and Hg^{2+} has also been practiced on the modified carbon electrode (GCE) for DPASV by using an amine functionalized graphene oxide..[7] Similarly, DPASV has also been performed for the simultaneous recognition of Cd^{2+}, Pb^{2+}, Cu^{2+}, and Hg^{2+}[8] by using gold nanoparticles (NPs) on the surface of GCE. Here, differential normal pulse voltammetry (DNPV) was used only for the simultaneous sensing/detection of HMIs because the simultaneous detection of HMIs using the DNPV technique results in strong intermetallic interaction; therefore, this method was not used in individual analysis.

Recently, for highly sensitive and selective recognition of HMIs, nanomaterials with various functionalities and accumulating abilities to adjust electrochemical electrodes for specific target HMIs have been reported.[9−15] Among them, Co_3O_4 is an important semiconductor oxide that has scientific application in energy storage and redox catalysis.[16] However, the concrete use of Co_3O_4 has been unfulfilled yet, mostly owing to particle aggregation, expansion−contraction in volume, poor cycling stability, and capacity loss.[17,18]

To enhance the electronic conductivity and to avoid aggregation, Co_3O_4 NPs have been used with carbon-based materials, such as amorphous carbon,[19] carbon nanofibers,[20] carbon nanotubes,[21,22] and graphene/reduced graphene oxide (rGO).[23−25] In particular, it has been verified that graphene/rGO not only improves the electronic conductivity but also

Received: October 26, 2021
Accepted: January 27, 2022
Published: February 11, 2022

https://doi.org/10.1021/acsomega.1c05989
ACS Omega 2022, 7, 5870−5882

Scheme 1. Design and Synthesis of rGO·Co_3O_4, rGO·PEI, and Porous rGO·Co_3O_4·PEI NCPs

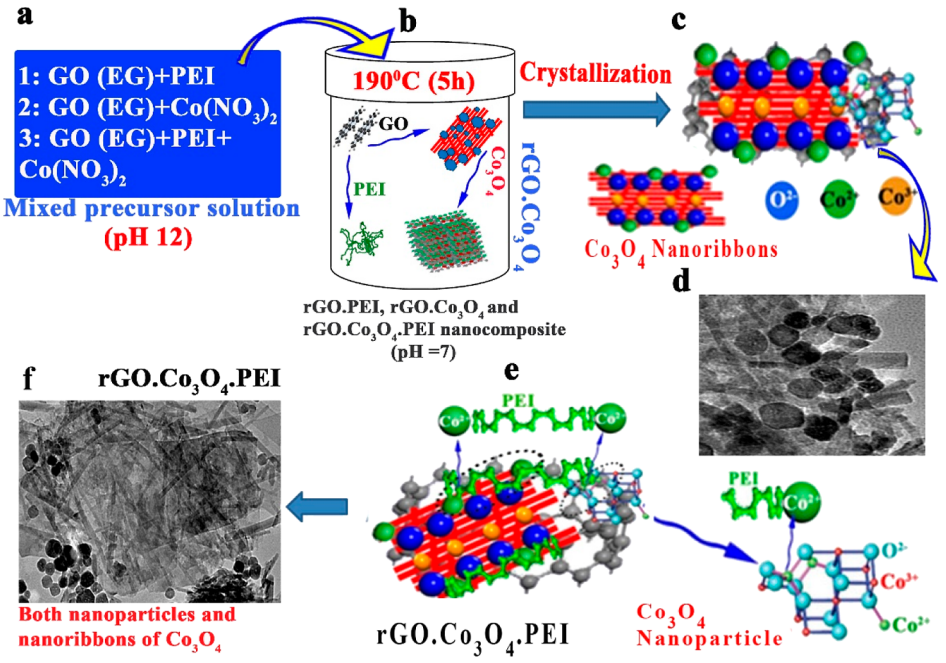

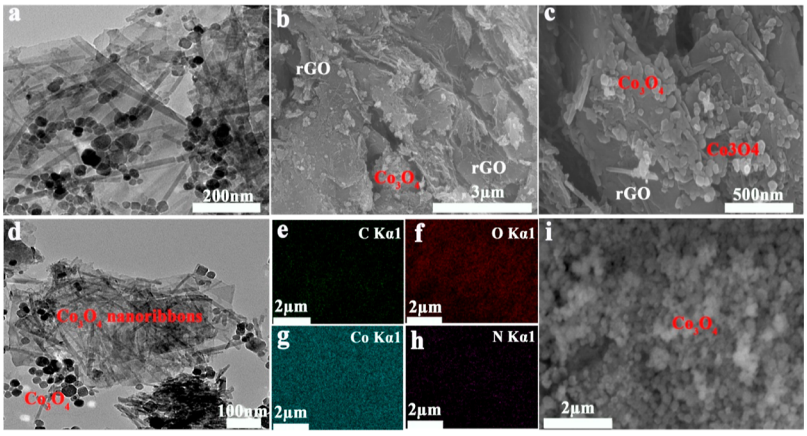

Figure 1. TEM and SEM images of the porous rGO·Co_3O_4·PEI NCP. (a,d) TEM images of rGO·Co_3O_4·PEI, (b,c,i) SEM images, and (e–h) EDS maps corresponding to (i).

prevents the aggregation of Co_3O_4 NPs. Thus, the design of the Co_3O_4/graphene composite is the most competent selection for progress of the electrochemical activity of Co_3O_4.[26,27]

As reported earlier,[28] the described N-doped PC-Co_3O_4 nanocomposite (NCP) that possesses numerous N functional groups deliver additional binding sites and improved electrochemical performance. The N-doped PC-Co_3O_4 NCPs have efficiently relieved the aggregation of Co_3O_4 and exhibited excellent cycle performance capacity. Similarly, graphene-based Co_3O_4 composites have obtainable stability, sustainability, high specific capacity, and excellent electrochemical performance.[29−31]

The most important characteristic of Co_3O_4 nanocrystals is their unsaturated surface atoms bound with supplementary atoms. These atoms have strong chemical activities to efficiently adsorb metal ions. Generally, Co^{3+} ions on the exterior are unimpregnated and bonded with several dangling bonds, which can produce catalytic active sites. Also, it is reported that the surface with extra dangling bonds possesses additional active sites and therefore has strong chemical activities.[32−34] This means that the direct nucleation, growth, and attachment of Co_3O_4 nanocrystals with a suitable support are responsible features in determining the catalytic behavior. Therefore, the exposed crystal facets of nanocrystals are believed to play a significant role in adjusting the overpotential for the reaction in different contexts. The present study focuses on the detection of HMIs and the effect of increased potential on voltammetry methods.[35] For Co_3O_4 nanocrystals, the facet-dependent electrochemical activities toward HMIs have also been reported. For example, the (111) facet of Co_3O_4 nanoplates is considered to be better than the (001) facet of Co_3O_4 nanocubes in electrochemical sensing.[36] Few studies have investigated HMI incorporation on active facets of Co_3O_4 nanoribbons to explore their stripping behavior by electrochemical methods.

In this work, we have tried to combine a conductive polymer polyethylenimine (PEI) with Co_3O_4 and rGO [from expandable graphite (EG)] to formulate an electrochemical platform for individual as well as simultaneous analysis of

https://doi.org/10.1021/acsomega.1c05989
ACS Omega 2022, 7, 5870−5882

HMIs (Cd^{2+}, Pb^{2+}, Cu^{2+}, and Hg^{2+}) in solution by applying stripping voltammetry (SWV) and DNPV methods, respectively. During the formation of rGO·Co_3O_4·PEI NCP, GO from EG was simultaneously reduced to rGO along with the precipitation of dense Co_3O_4[26] with good electron transport property. Meanwhile, PEI was fabricated hydrothermally with less active site Co^{2+} to enhance the interaction between Co_3O_4 and rGO. Moreover, the conductive polymer PEI possesses a lot of N functional groups that provide more binding sites to detect HMIs. Most importantly, we designed a thin Co_3O_4 nanoribbon structure with active planes of (110) and (220)[37,38] to enhance the activity as well as the stability of Co_3O_4. The design strategy for the formation of a porous rGO·Co_3O_4·PEI NCP is given in Scheme 1. This porous rGO·Co_3O_4·PEI NCP with thin Co_3O_4 nanoribbons was found to be a favorable material for the electrochemical detection of HMIs.

2. RESULTS AND DISCUSSION

2.1. Characterization of the Porous rGO·Co_3O_4·PEI NCP. *2.1.1. Structure and Morphology of the rGO·Co_3O_4·PEI NCP.* The methods for the preparation of rGO·Co_3O_4·PEI-1, rGO·Co_3O_4·PEI-2 NCP, and rGO·PEI NCP are summarized in the Supporting Information. The morphology of rGO·PEI, rGO·Co_3O_4·PEI-1, rGO·Co_3O_4·PEI-2, and rGO·Co_3O_4·PEI NCP was analyzed by transmission electron microscopy (TEM) (Figures 1, 2 and S1−S6), scanning electron microscopy (SEM), and energy-dispersive X-ray spectroscopy (EDS).

TEM images in Figure 1a illustrate a porous rGO·Co_3O_4·PEI NCP structure with both nanoribbons and Co_3O_4 NPs covered by the conducting layer of PEI. Both NPs and nanoribbons can be easily seen in Figure 1a,d. The dense Co_3O_4 NPs ranging from 18 to 47 nm covering the rGO layer can be seen in Figure S3. As shown in Figure 1c,e−h, the EDS mapping elucidates the occurrence of all elements C, O, Co, and N in the rGO·Co_3O_4·PEI NCP. The well-bonded N atom of the conducting polymer PEI in porous rGO·Co_3O_4·PEI NCP provides more active sites due to the heterojunction among rGO and Co_3O_4. Thus, it is expected to be used as an electrochemical sensor.

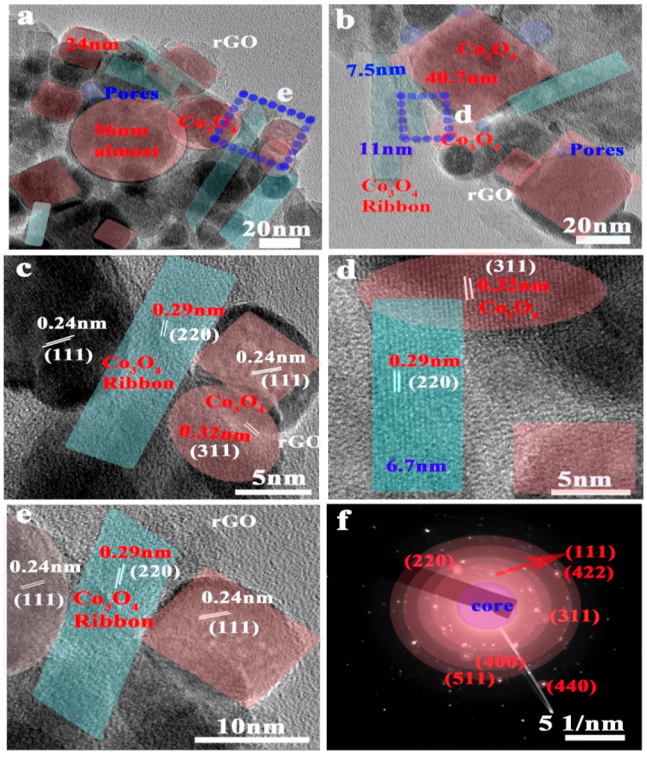

Figure 2. TEM and HRTEM images of the porous rGO·Co_3O_4·PEI NCP. (a−c) TEM images of rGO·Co_3O_4·PEI, (d,e) HRTEM images of rGO·Co_3O_4·PEI, and (f) selected-area electron diffraction (SAED) pattern of rGO·Co_3O_4·PEI.

For rGO·Co_3O_4·PEI NCP, the graphene layers acting as a substrate, Co_3O_4, and the conducting layer of PEI in the porous rGO·Co_3O_4·PEI NCP are clearly seen in Figures 1, 2, S3, and S4. The Co_3O_4 NPs and thin nanoribbons are confirmed by TEM and high-resolution TEM (HRTEM) on the surface of rGO and can be clearly seen in Figures 2a−e and S3e,f. The pores in the rGO·Co_3O_4·PEI NCP can be clearly seen in Figure S3c,d. The EDS spectrum (Figure S3g) further confirms the formation of the porous rGO·Co_3O_4·PEI NCP with weight (%) for Co, O, C, and N of 68, 27, 3, and 1%, respectively. This indicates that rGO·Co_3O_4 is covered by a thin conducting layer of PEI, as presented in Figures S1−S4.

The lattice fringe spacings of ∼0.29 and 0.46−0.54 nm (Figures 2c−e, 3g,i, S6d−f, S3, and S4) correspond to (220) and (110) planes of the Co_3O_4 nanoribbon and 0.24 and 0.32 nm for (111) and (311) planes of cubic Co_3O_4, respectively. The thin nanoribbon Co_3O_4 of 6.5−11 nm width (Figure 2b,d) and cubic Co_3O_4 crystals of 24−56 nm size can be clearly indicated in Figures 2a,b, S3, and S4.

The TEM images of the porous rGO·Co_3O_4·PEI-1 NCP illustrate that when the $Co(NO_3)_2$ solution concentration was turned down to half, less nanoribbon/nanorod structures were obtained compared to rGO·Co_3O_4·PEI (Figure S4). TEM images also show a porous structure (Figure S4f). As shown in Figure S6d,f, the Co_3O_4 nanoribbon or nanorod shows a (220) plane. Therefore, it can be deduced that the Co_3O_4 nanoribbon primarily grows along the {110} or {220} direction and favorably displays the (110) or (220) planes (Figures 3 and S6). Co_3O_4 has a spinel structure with Co^{3+} attached with six oxygen atoms in an octahedral relationship (Figure S6b) and Co^{2+} in a tetrahedral coordination (Figure S6c). The previous Co^{3+} is considered as the active site, while the last is nearly inactive.[38,40] The compact planes are (220), (111), and (110) with their surface atomic arrangements as presented in Figure 3a−c. It has been proved that the (111) plane comprises Co^{2+} cations, whereas the (220) and (110) planes are mainly imperturbable Co^{3+} cations. Actually, the surface differential diffraction research has proved that Co^{3+} cations exist merely on the (110)/(220) plane.[41−43] Further information about the nanoribbon Co_3O_4 flat top, atomic plane, and side plane can be found in Co_3O_4 nanorod formation.[44,45] The planar density for the (111) plane is 0.185 × 10^{20} atoms nm^{-2} (Figure S7), and for the (110) and (220) planes, it is 0.113 × 10^{20} and 0.113 × 10^{20} atoms nm^{-2}, respectively.

The TEM results illustrated in Figures 2, 3, S3, and S4 are in accordance with X-ray diffraction (XRD) spectra. Figure 2f displays the SAED configuration of the porous rGO·Co_3O_4·PEI NCP. The diffraction rings of (220) are in agreement with the Co_3O_4 nanoribbon, and the (111), (311), (400), (422), (511), and (440) planes correspond to Co_3O_4 NPs, demonstrating the presence of Co_3O_4 crystals (JCPDS. no 42-1467)[46−49] in the rGO·Co_3O_4·PEI NCP.

https://doi.org/10.1021/acsomega.1c05989
ACS Omega 2022, 7, 5870−5882

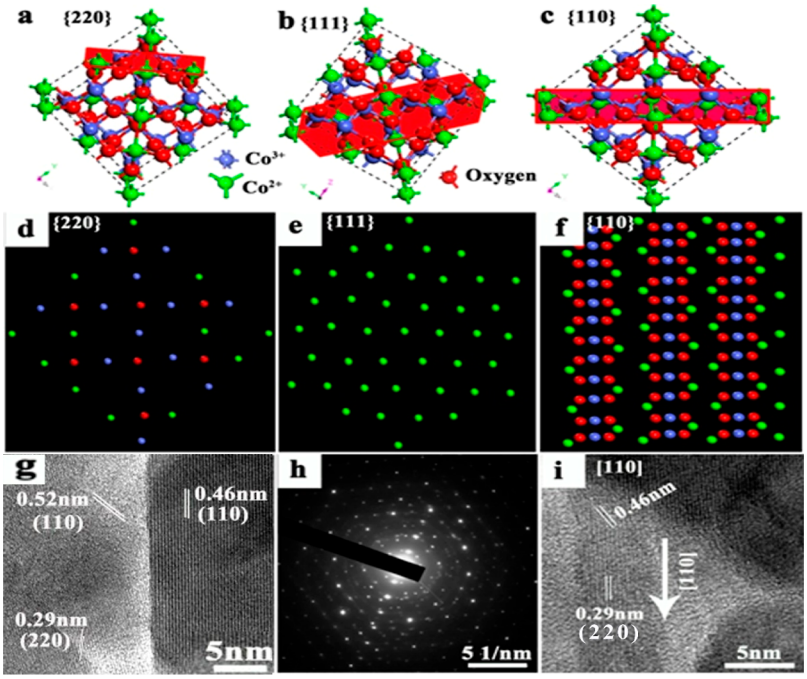

Figure 3. Co_3O_4 nanoribbon/NP crystal plane structure and HRTEM images of rGO·Co_3O_4·PEI. (a−c) Surface atomic configuration of Co_3O_4 in (220), (111), and (110) planes, (d−f) surface atomic textures in the (220), (111), and (110) planes, (g) HRTEM image illustrating the (220) and (110) planes of the Co_3O_4 nanoribbon/NP on rGO·Co_3O_4·PEI, (h) SAED pattern of the Co_3O_4 (111) plane on rGO·Co_3O_4·PEI, and (i) crystal growth along the (110) plane of the Co_3O_4 nanoribbon on rGO·Co_3O_4·PEI.

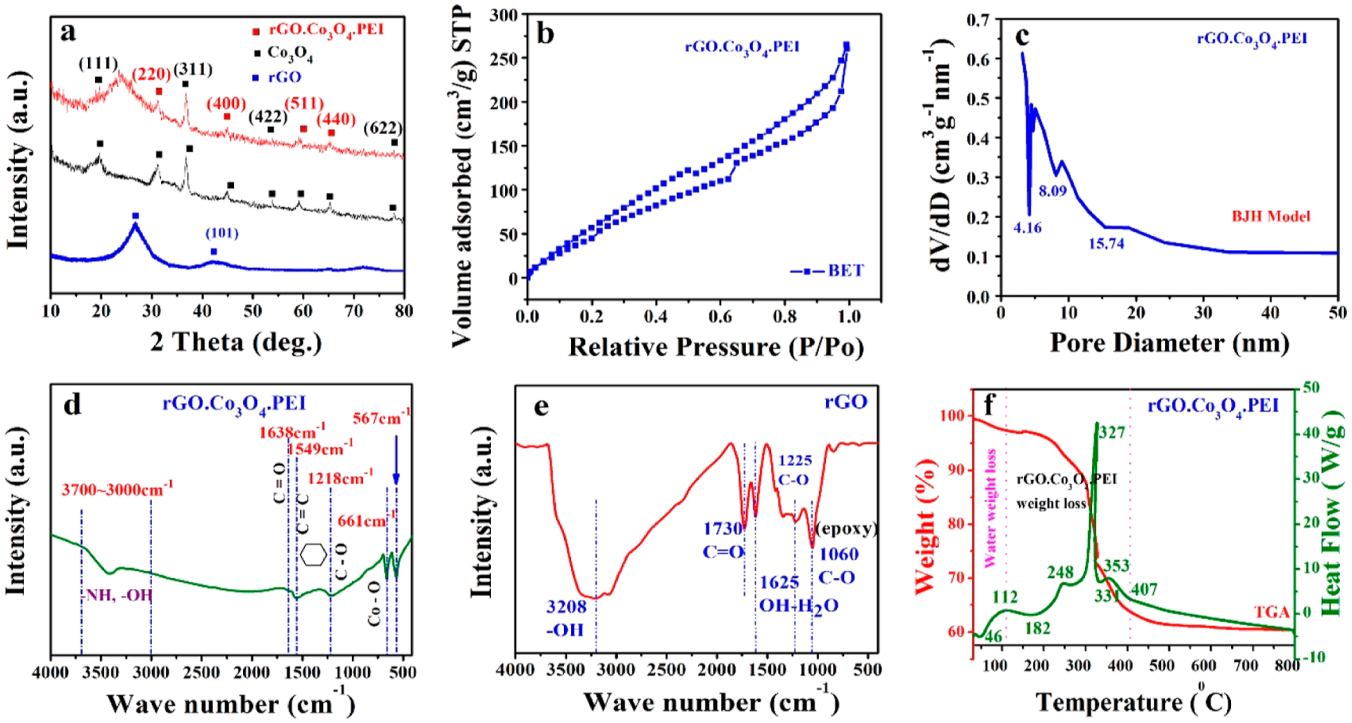

Figure 4. XRD pattern of the rGO·Co_3O_4·PEI NCP (a), BET and pore size distribution (b,c), FTIR spectra (d,e), and TGA curve (f).

2.1.2. Characterization of the rGO·Co_3O_4·PEI NCP. The crystal structures of rGO, Co_3O_4, and rGO·Co_3O_4·PEI were characterized by XRD (Figure 4a). The characteristic curving peaks appear at 26.59 and 44.86° attributed to the (002) and (101) planes of rGO and the peaks at 19.6, 31.24, 36.63, 44.86, 59.14, and 65.17° confirm the (111), (220), (311), (400), (511), and (440) crystalline planes of Co_3O_4, respectively (JCPDS no. 42-1467).[49−51] The broad curve in the XRD pattern at 23.59° is recognized as the construction of layers in the rGO·Co_3O_4·PEI NCP, which is in accordance with HRTEM and TEM images (Figures 1 and 2).[52,53]

N_2 adsorption/desorption was performed to study the pore size distribution and surface areas of the porous rGO·Co_3O_4·PEI NCP (Figure 4b,c). The porous rGO·Co_3O_4·PEI NCPs

https://doi.org/10.1021/acsomega.1c05989
ACS Omega 2022, 7, 5870−5882

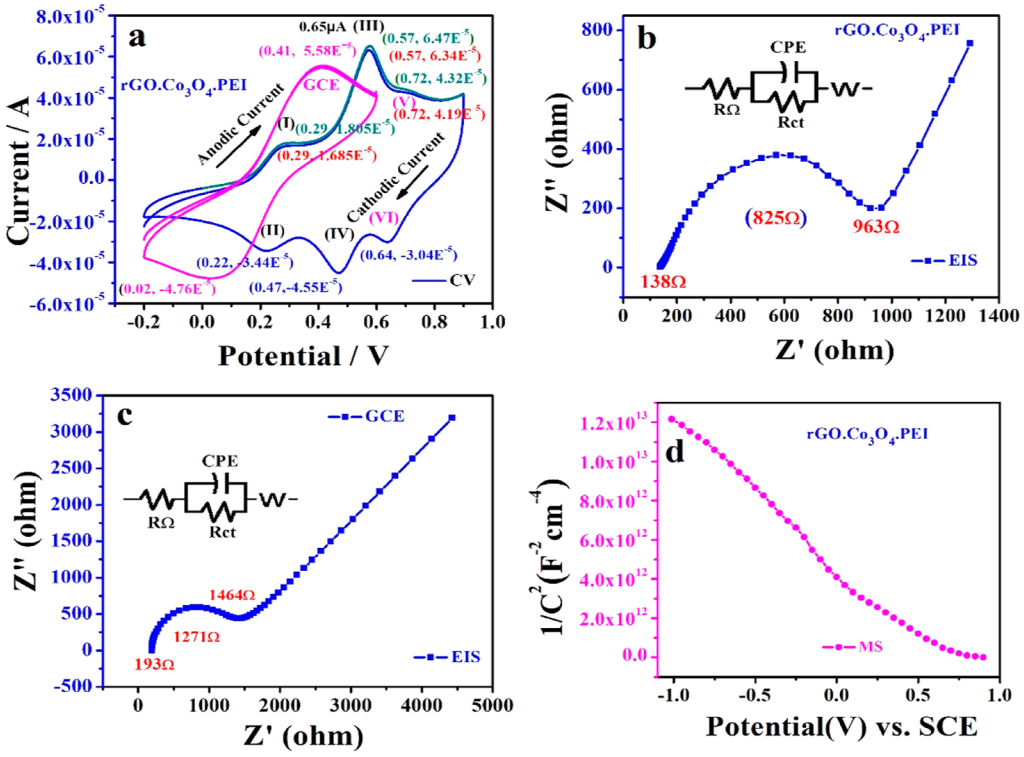

Figure 5. CV curves (a), EIS curves (b,c), and MS plots (d) of rGO·Co_3O_4·PEI NCP (5 mM $Fe(CN)_6^{3-/4-}$, 1 M KCl, 1 M NaAc−HAc, pH 5 ± 02, 0.1 mV s^{-1}).

possess a BET surface area of 261.15 cm^3 g^{-1} with a total pore volume of 0.612 cm^3 g^{-1}. As illustrated in Figure 4c, the average pore size of the porous rGO·Co_3O_4·PEI NCP was 9.4 nm, in close resemblance with the reports of t N-doped macroporous and mesoporous graphene-based metal oxides and N-doped PC NCPs.[54,55]

The Fourier-transform infrared (FTIR) spectra of rGO and rGO·Co_3O_4·PEI NCP (Figure 4d,e) were recorded to additionally explore the property of the porous rGO·Co_3O_4·PEI NCP. The widespread absorption peaks at 3000−3700 cm^{-1} are ascribed to the −NH and −OH groups in the rGO·Co_3O_4·PEI NCP. Similarly, the peak at 1625 cm^{-1} is assigned to the −OH bending vibration of absorbed water molecules, and the involvement of aromatic C═C (1218 and 1225 cm^{-1}) further confirms the successful reduction of GO.[56] The peaks at 567 and 661 cm^{-1} are allotted to Co−O vibrations. The FTIR study additionally confirms that Co_3O_4 NPs are effectively deposited on the surfaces of rGO.[57−61]

Figures 4f and S8 show the thermogravimetric analysis (TGA) curve of rGO·Co_3O_4·PEI NCP. The weight loss observed below 112 °C is generally recognized to be due to dehydration or drying out of the NCP. The additional weight loss phase from 112 to 407 °C is due to the decomposition of the rGO·Co_3O_4·PEI NCP, and the temperature range after almost 500 °C might be ascribed to Co_3O_4. On the basis of the TGA curve, the loss in the weight ratio of rGO·Co_3O_4·PEI NCPs of about 40 wt % is almost similar to the result reported[62] for the formation of the Co_3O_4−carbon composite.

2.2. Electrochemical Characteristics of rGO and rGO·Co_3O_4·PEI NCP. *2.2.1. Cyclic Voltammetry, Electrochemical Impedance Spectroscopy, and Mott−Schottky Measurements of the rGO·Co_3O_4·PEI NCP.* The cyclic voltammetry (CV), electrochemical impedance spectroscopy (EIS), and Mott−Schottky (MS) measurements of the rGO·Co_3O_4·PEI-modified electrodes were carried out in a solution of 5 mM $Fe(CN)_6^{3-/4-}$, 1 M KCl using the $Fe(CN)_6^{3-/4-}$ redox couple, and —1 M NaAc−Hac was used to adjust the pH to 5.0. The results are shown in Figure 5.

As shown in Figure S11a, both the anodic (0.27 V) and cathodic (0.18 V) peaks of GO are less compressed than those of rGO, rGO·PEI, and rGO·Co_3O_4-modified electrodes. The electrochemical gaps are adjusted to the spots of the redox couples. It can be sensed that at the anodic current curve of the rGO·Co_3O_4-modified electrode, there are two redox couples from 0.2 to 0.6 V/s. They are sited at 0.27/0.56 V/s and 0.63/0.45 V/s, respectively. As presented in Figure 5a, both the anodic (0.41 V) and cathodic (0.02 V) peak of GCE are less thick/broad than those of the rGO·Co_3O_4·PEI-modified electrode. The peaks around 0.29 (I) and 0.57 V (III) in the first cycle are ascribed to the decline of Co_3O_4 to Co along with the construction of a solid electrolyte edge as well as the development of a solid electrolyte connection reaction on the exterior of the rGO·Co_3O_4·PEI NCP (same as that reported[63,64] for the Co_3O_4 nanowall in Li-ion batteries). At the anodic current curve, two redox couples are detected from 0.2 to 0.6 V/s. They are positioned at 0.22/0.47 V and 0.57/0.647 V, respectively, arising due to the reversible conversion attributed to Co_3O_4 and CoOOH(II/III) and similar reversible conversions between CoOOH and CoO_2(III/IV).[57,62,65] The peaks at 0.72 (V) and 0.29 V (I) in the first cycle are ascribed to the depletion of Co_3O_4 to Co, along with the development of a solid electrolyte edge on the exterior of rGO·Co_3O_4·PEI, with 0.65μA current greater than GCE, as shown in Figure 5a.[65]

The porous PEI-functionalized Co_3O_4/rGO NCPs were characterized by X-ray photoelectron spectroscopy (XPS) spectrum as shown in Figure S13. The strong peaks at 287.9, 400, 538.2, and 783.2 eV analogous to the distinct peaks of C

https://doi.org/10.1021/acsomega.1c05989
ACS Omega 2022, 7, 5870−5882

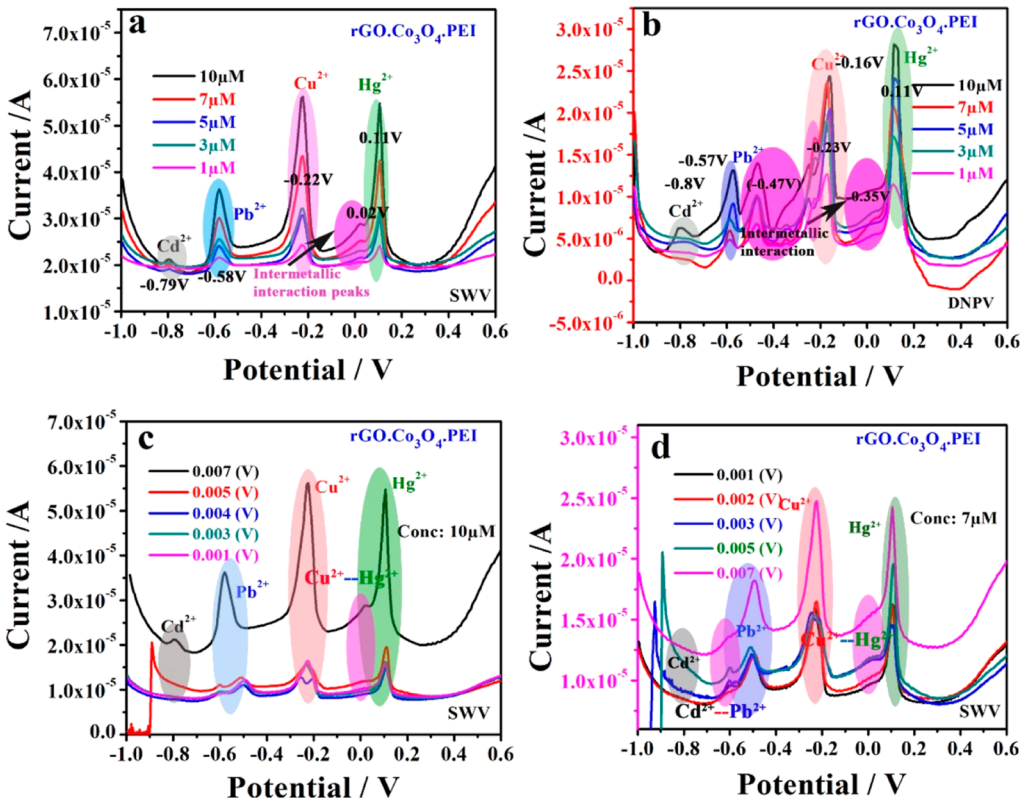

Figure 6. SWV and DNPV results of rGO·Co_3O_4·PEI NCP, (a) SWV curves and (b) DNPV curves from 1 to 10 μM with an increased potential of 0.007 V (7 mV) for SWV and an increased potential of 0.001 V (1 mV) for DNPV, (c,d) increased potential of 0.001−0.007 V for SWV at 10 and 7 μM, respectively (pH, 5 ± 02).

1s, N 1s, O 1s, and Co 2p indicate the presence of C, N, O, and Co elements, respectively, in the sample. The Co $2p_{1/2}$ and Co $2p_{3/2}$ spectra can be deconvoluted into four peaks at 794.8 and 793.2 eV for Co $2p_{1/2}$, 782.7 and 781.4 eV for Co $2p_{3/2}$, showing the characteristic of the Co_3O_4 phase (Figure S13b). Similarly, for co-doping of graphene with Co_3O_4 and PEI O 1s and N 1s spectrum linkage and interaction with graphene and Co_3O_4 shown in Figure S13c,d confirm rGO·Co_3O_4·PEI NCP.

The EIS experiments were performed between −0.2 and 0.6 V at room temperature, as illustrated in Figure 5b,c. Figure 5b shows Nyquist plots of GCE and rGO·Co_3O_4·PEI (Figure 5c). It might be perceived that the rGO·Co_3O_4·PEI electrode has the smallest diameter (825 Ω), compared to GO (2868 Ω), GCE (1271 Ω), and rGO·Co_3O_4 (1849 Ω) (Figure S11b), signifying that the rGO·Co_3O_4·PEI-modified electrode possesses a smaller R_{ct} value than GCE (Table S1). The results show that the electrochemical reaction on the surface of anode/electrolyte for rGO·Co_3O_4·PEI is more prominent than that on the GCE electrode, which is almost the same as reported by ref 57 for the Co_3O_4/rGO-0.50 electrode. Meanwhile, the film resistance and resistance of charge transfer (R_S and R_{ct}) of the rGO·Co_3O_4·PEI NCP are lower than those of GCE (Table S1). Further suitable results are displayed in Table S1, indicating that the R_S (135.6 Ω) and R_{ct} (419.7 Ω) of the rGO·Co_3O_4·PEI NCP-modified electrode are lesser in comparison with those of the pure GCE electrode (193 and 1070 Ω, respectively).

The rGO·Co_3O_4·PEI NCP exhibited a negative (adverse) slope for the MS plot and hence exhibit a p-type semiconducting performance, as illustrated in Figure 5d and Table S2; the carrier density (N_{ds}) of rGO·Co_3O_4·PEI NCP was calculated as 1.56×10^{18} (with a quiet time of 2 s, an amplitude of 0.005 V, and an increased potential of 0.05 V).

2.2.2. SWV and DNPV Voltammetry Analyses Intended for the Sensing/Detection of Cd^{2+}, Pb^{2+}, Cu^{2+}, and Hg^{2+} by Means of the rGO·Co_3O_4·PEI-Modified Electrode. SWV and DNPV electrochemical analyses were used to detect the four HMIs (Cd^{2+}, Pb^{2+}, Cu^{2+}, and Hg^{2+}). Figure 6a,b illustrates the SWV and DNPV peaks from 1 to 10 μM concentration of Cd^{2+}, Pb^{2+}, Cu^{2+}, and Hg^{2+} aqueous solutions with an increased potential of 7 mV for SWV and 1 mV for DNPV at pH 5 ± 02. For the stripping analysis of HMIs using both SWV and DNPV, the obtained results in the form of voltammetric peaks are shown in Figure 6a,b, and the rGO·Co_3O_4·PEI NCP was subject to the simultaneous investigation of HMIs. The vertices at almost −0.79, −0.58, −0.22, and 0.11 V are assigned to Cd^{2+}, Pb^{2+}, Cu^{2+}, and Hg^{2+} on SWV, respectively (Figure 6a); similarly, the peaks at almost −0.801, −0.573, −0.162, and 0.114 V are allocated to Cd^{2+}, Pb^{2+}, Cu^{2+}, and Hg^{2+}, respectively, on DNPV analysis. The peaks at 0.02 V for SWV and −0.35 V for DNPV between Cu^{2+} and Hg^{2+} (Figure 6a,b) are assigned to the occurrence of inter-metallic interactions.[66,67]

Figure 6c shows the increased potential from 0.001 to 0.007 V for the SWV analysis at 10 μM concentrations of four HMIs (Cd^{2+}, Pb^{2+}, Cu^{2+}, and Hg^{2+}). Similarly, Figure 6d illustrates the increased potential of 0.001−0.004 V for SWV at 7 μM concentration. The peaks at an increased potential of 0.007 V (7 mV) are recommended to be the best for the 1−10 μM concentration of Cd^{2+}, Pb^{2+}, Cu^{2+}, and Hg^{2+} for both individual (Figure S9) and simultaneous analyses of SWV (Figure 6c,d). Figure S9 illustrates the individual analysis of the

https://doi.org/10.1021/acsomega.1c05989
ACS Omega 2022, 7, 5870−5882

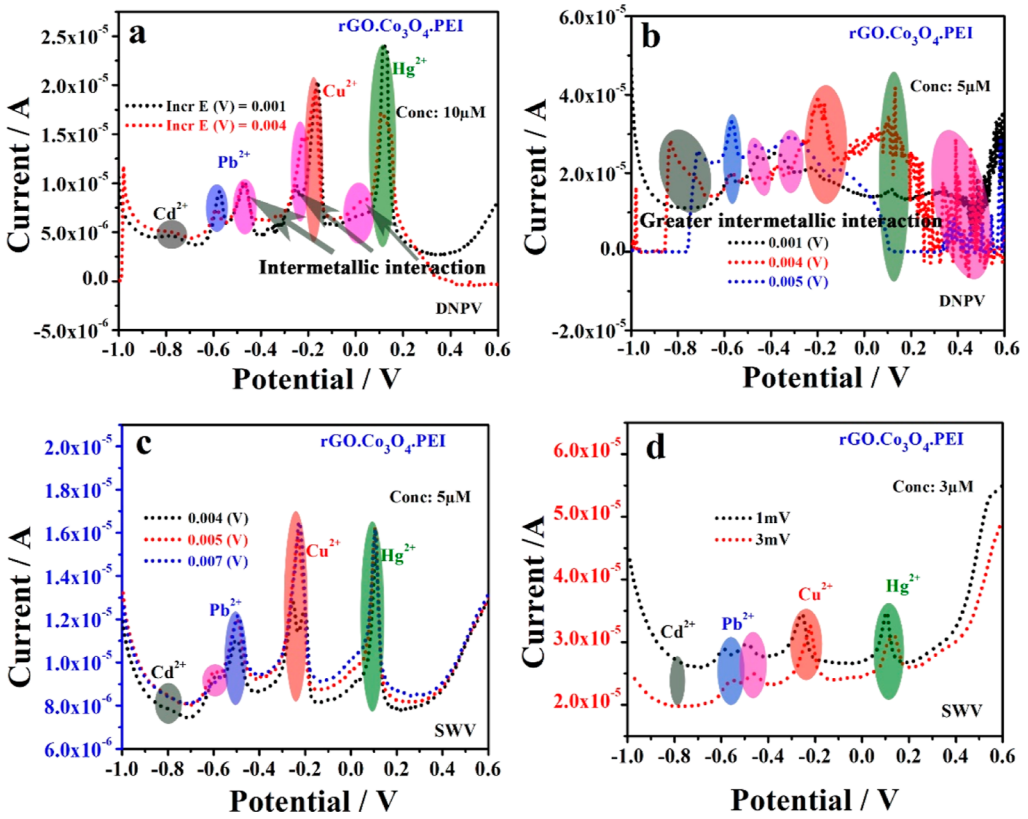

Figure 7. Voltammetric curves (a,b) for the increased potential of 0.001−0.007 V for DNPV at 10 μM and 5 μM concentrations, respectively, for simultaneous analysis, (c) for the increased potential of 0.004−0.007 V for SWV at 5 μM concentration, and (d) for the increased potential of 0.001 V (1 mV) and 0.003 V (3 mV) carried out on SWV at 3 μM concentration.

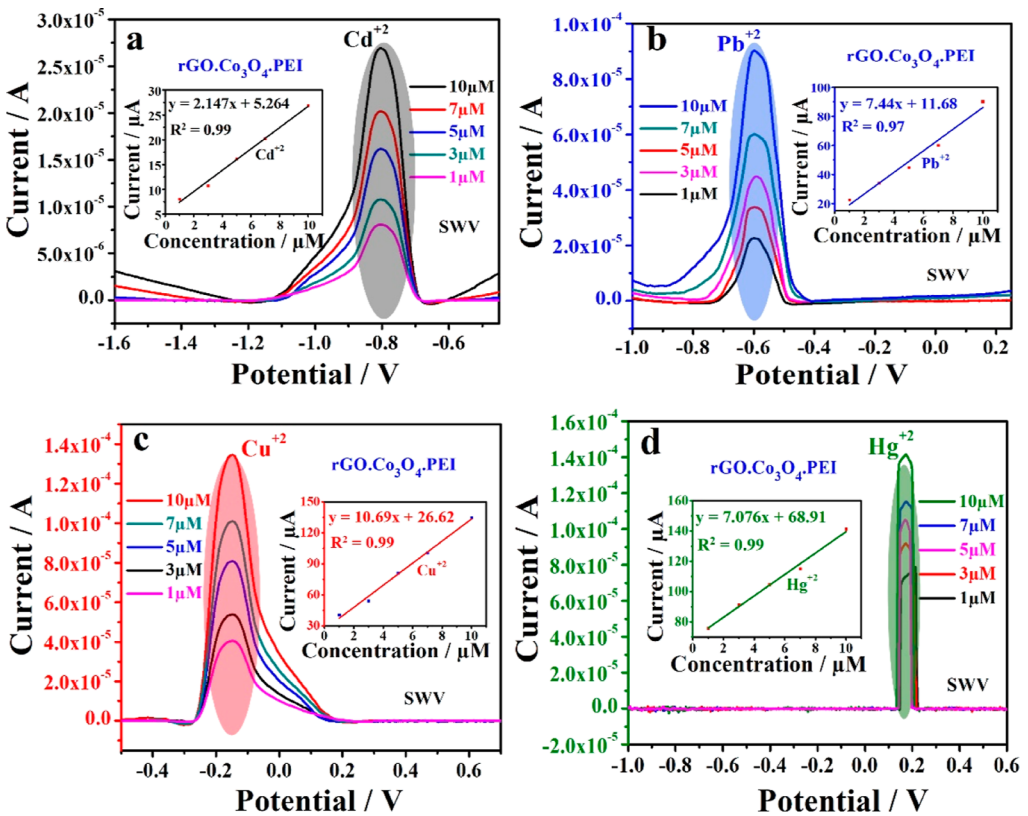

Figure 8. SWV response of the rGO·Co_3O_4·PEI NCP-modified electrode and calibration curves for the individual investigation of (a) Cu^{2+}, (b) Hg^{2+}, (c) Pb^{2+}, and (d) Cd^{2+} in the 1−10 μM concentration range, while other parameters were the same as in Figure 6 in acetate buffer (0.1 M).

https://doi.org/10.1021/acsomega.1c05989
ACS Omega 2022, 7, 5870−5882

Scheme 2. Mechanism of Detection of HMIs by Using the rGO·Co_3O_4·PEI NCP; (a) Interaction of PEI with Co^{2+} on rGO·Co_3O_4·PEI, (b) Co_3O_4 NP Interaction with HMIs on rGO·Co_3O_4·PEI, and (c) Detection of HMIs and the Interaction between PEI, rGO, and Co_3O_4 with HMIs

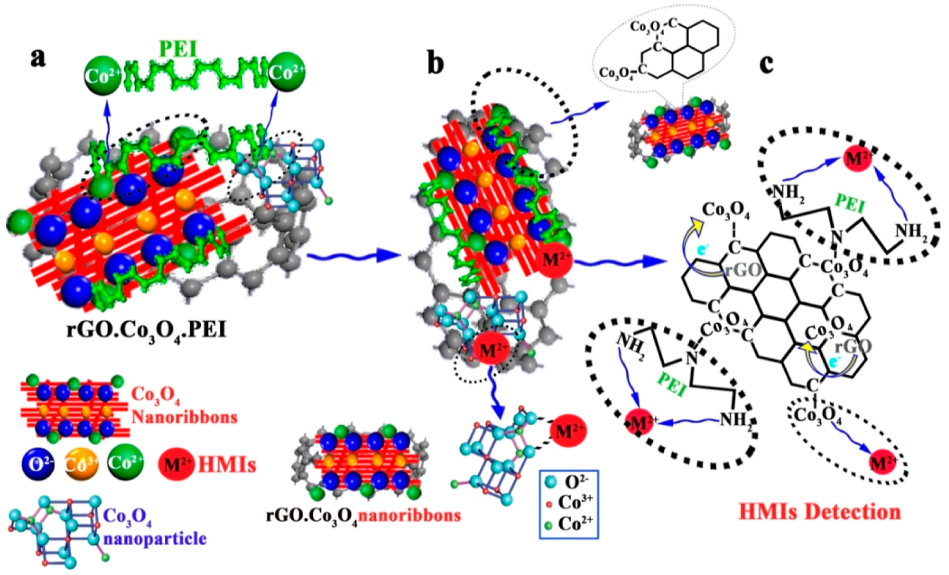

rGO·Co_3O_4·PEI NCP for SWV. Figure S9a illustrates it for Cu^{2+} (1 μM) with an increased potential from 0.001 to 0.007 V (1 mV) and Figure S9b illustrates the same for Cu^{2+} (3 μM) with an increased potential from 0.007 (7 mV) to 0.049 V, demonstrating that 7 mV potential is the best for the individual measurement of Cd^{2+}, Pb^{2+}, Cu^{2+}, and Hg^{2+}. The sensing performance of rGO, rGO·PEI, and rGO·Co_3O_4 NCPs was satisfactory but not strong enough as that of the rGO·Co_3O_4·PEI NCP (Figure S12).

To check the increased potential effect on voltammetric peaks, the potential was varied from 1 to 7 mV; when the potential was increased from 1 to 5 mV, the intensity of voltammetry peaks increased a little. However, the voltammetry spectrum becomes better than before at an increased potential of 7 mV. Therefore, an increased potential of 7 mV is recommended to be the best for the simultaneous sensing/detection of Cd^{2+}, Pb^{2+}, Cu^{2+}, and Hg^{2+} on SWV, as shown in Figure 6c,d.

2.2.3. Increased Potential Effect on the Voltammetry Spectrum. Figure 7 shows the increased potential effect on SWV peaks for both SWV and DNPV analyses. The increased potential effect from 0.001 to 0.005 V for DNPV at 10 and 5 μM for simultaneous analysis is shown in Figure 7a,b. When the potential was increased from 1 to 5 mV, the intermetallic interaction increased, and almost three new voltammetry peaks at −0.47, −0.23, and 0.001 V were observed, which is shown in pink with other parameters in Figure 7a,b. Figure 7c,d illustrates the effect of the increased potential of 4−7 mV for SWV at 5 μM concentration and 1 and 3 mV for SWV at 3 μM concentration. The vertices at −0.799, −0.599, −0.23, and 0.11 V are attributed to Cd^{2+}, Pb^{2+}, Cu^{2+}, and Hg^{2+}, respectively; the intensity of voltammetric peaks increases with the increase in potential from 1 to 7 mV (Figure 7c,d). However, two stronger intermetallic interactions between Pb^{2+}−Cu^{2+}[68] and Cu^{2+}−Hg^{2+}[69] at −0.49 and 0.011 V were also observed for SWV measurements. Similarly, the less intense peaks arise at 0.02 V for SWV and −0.35 V for DNPV between Cu^{2+} and Hg^{2+} (Figure 6a,b), which are due to the occurrence of inter-metallic interactions.[69] Due to stronger intermetallic interactions, the DNPV voltammetry method was not proceeded further. However, at an increased potential of 1 mV for simultaneous DNPV analysis, the limit of detection (LOD) and sensitivity were found to be good (Table S4).

2.3. Stripping Analysis of Pb^{2+}, Cd^{2+}, Hg^{2+}, and Cu^{2+}. *2.3.1. Individual Depriving Performance Analysis for Cd^{2+}, Cu^{2+}, Hg^{2+}, and Pb^{2+} Using SWV.* The SWV response of the rGO·Co_3O_4·PEI-modified electrode (GCE), linearization equations, and calibration curves for the individual voltammetry examination of Cd^{2+}, Pb^{2+}, Cu^{2+}, and Hg^{2+} from 1 to 10 μM concentration are presented in Figure 8a−d and Table S5.

The respective calibration curves of rGO·Co_3O_4·PEI for the simultaneous sensing/detection of Cd^{2+}, Pb^{2+}, Cu^{2+}, and Hg^{2+} corresponding to Figure 6a are shown in Figure S10 and Table S3. For Cd^{2+}, Pb^{2+}, Cu^{2+}, and Hg^{2+}, the inevitable LODs were 0.285, 1.13, 1.19, and 1.29 nM for SWV (Table S3); similarly, they were 1.07, 0.285, 2.40, and 1.12 nM for DNPV (Table S4) for simultaneous detection, whereas they were 0.484, 0.878, 0.462, and 0.477 nM for SWV (Table S5) for individual analysis of Cd^{2+}, Pb^{2+}, Cu^{2+}, and Hg^{2+}. The linearization equation and the calculation of the corresponding coefficients for concurrent determination of Cd^{2+}, Pb^{2+}, Cu^{2+}, and Hg^{2+} are enumerated in Tables S6 and S7.

As shown in Figure S10, the corresponding calibration curves for Cd^{2+}, Pb^{2+}, Cu^{2+}, and Hg^{2+} for simultaneous analysis by SWV were built from 1 up to 10 μM. Similarly, the corresponding calibration curves for the four HMIs (inset in Figure 8 and Table S6) represent the linearization equations with comparable correlation coefficients of 0.99, 0.97, 0.99, and 0.98 for individual analysis by SWV when the rGO·Co_3O_4·PEI NCP was employed. The LODs for simultaneous sensing/detection of Cd^{2+}, Pb^{2+}, Cu^{2+}, and Hg^{2+} with the use of the rGO·Co_3O_4·PEImodified electrode were estimated to be 0.285, 1.13, 1.19, and 1.29 nM for SWV (Table S3); similarly, they were 1.07, 0.285, 2.40, and 1.12 nM for DNPV (Tables S4 and S7) during simultaneous detection (3σ method), respectively. The fallouts acquired by the use of the rGO·Co_3O_4·PEI NCP for LOD in both DNPV and SWV voltammetry analyses were found to be inferior to the values

https://doi.org/10.1021/acsomega.1c05989
ACS Omega 2022, 7, 5870−5882

recommended by the World Health Organization (WHO) (see Table S8).

2.4. Sensitivity and LOD Calculation of the rGO·Co_3O_4·PEI NCP. For individual analysis with the SWV voltammetric method, the sensitivities of the rGO·Co_3O_4·PEI-modified electrode calculated for Cd^{2+}, Pb^{2+}, Cu^{2+}, and Hg^{2+} are 3.50, 9.60, 13.9, and 14.6 μA/μM (Table S9). The lowest detectable (LOD) concentrations of Cd^{2+}, Pb^{2+}, Cu^{2+}, and Hg^{2+} for rGO·Co_3O_4·PEI reach 0.484, 0.878, 0.462, and 0.477 nM, respectively. For simultaneous analysis by SWV, the sensitivities of the rGO·Co_3O_4·PEI-modified electrode calculated for Cd^{2+}, Pb^{2+}, Cu^{2+}, and Hg^{2+} are 1.30, 2.70, 4.50, and 6.30 μA/μM, respectively, while the lowest measurable concentrations of Cd^{2+}, Pb^{2+}, Cu^{2+}, and Hg^{2+} by rGO·Co_3O_4·PEI are 0.285, 1.130, 1.190 and 1.29 nM, respectively. Similarly, for simultaneous analysis by DNPV, the sensitivities of the rGO·Co_3O_4·PEI-modified electrode calculated for Cd^{2+}, Pb^{2+}, Cu^{2+}, and Hg^{2+} are 1.20, 1.20, 2.90, and 2.60 μA/μM, respectively; while the lowest measurable concentrations of Cd^{2+}, Pb^{2+}, Cu^{2+}, and Hg^{2+} detected by rGO·Co_3O_4·PEI are calculated as 1.07, 0.285, 2.40, and 1.12 nM, respectively.

A comparison of the rGO·Co_3O_4·PEI NCP with previous work for the sensing/detection of Cd^{2+}, Pb^{2+}, Cu^{2+}, and Hg^{2+} is shown in Table S10. It can be illustrated from the present work that the porous rGO·Co_3O_4·PEI-modified electrode with a PEI thin cover on the exterior of the rGO·Co_3O_4 and Co_3O_4 nanoribbon structure has improved the sensitivity for both individual analysis and simultaneous analysis of Cd^{2+}, Pb^{2+}, Cu^{2+}, and Hg^{2+} in 1−10 μM concentration. The HRTEM images reveal that the Co_3O_4 nanoribbons mainly have (110) and (220) planes, preferring the occurrence of active Co^{3+} species on the surface. This might interact with HMIs directly, and the Co^{2+} plane will interact with the PEI thin film. The mechanism for the detection of HMIs by using rGO·Co_3O_4·PEI is shown in Scheme 2. For the porous rGO·Co_3O_4·PEI NCP, the conducting polymer PEI on the surface of Co_3O_4 nanoribbons and rGO (from EG) possessing a lot of N functional groups can provide more binding sites to bond with the objective HMIs and hence improve the electrochemical performance. Also, the Co_3O_4 nanoribbons with active (110) and (220) planes possess exclusive properties such as high electrical conductivity and chemical sensitivity and the ability to adsorb HMIs. The Co_3O_4 nanoribbons and NPs well dispersed on thin-layer rGO nanosheets can effectively buffer the disturbance initiated by structural and volume variations of Co_3O_4 nanoribbons and NPs, which might efficiently relieve or prevent Co_3O_4 NPs from aggregation. Thus, the design of the rGO·Co_3O_4·PEI NCP is one of the impressive ways to carry out the electrochemical routine of Co_3O_4.

Furthermore, the porous structure of the rGO·Co_3O_4·PEI NCP can allow the solution of HMIs to easily accumulate the target metal ions on the electrode surface, thereby showing excellent sensing performance. This new nanomaterial will be helpful in both laboratory and industrial scale applications.

3. CONCLUSIONS

In the present work, we tried to formulate an electrochemical method by combining the conducting polymers PEI and Co_3O_4 nanoribbons/NPs with rGO for the analysis of four selected (Cd^{2+}, Pb^{2+}, Cu^{2+}, and Hg^{2+}) HMIs in a solution by SWV and DNPV for the first time. For the SWV method, by simultaneous analysis (3σ method) LODs of Cd^{2+}, Pb^{2+}, Cu^{2+}, and Hg^{2+} using the rGO·Co_3O_4·PEI NCP-modified electrode are 0.285, 1.132, 1.194 and 1.293 nM, respectively; similarly, LODs are 1.069, 0.285, 2.398, and 1.115 nM for DNPV, , respectively whereas they are 0.484, 0.878, 0.462, and 0.477 for SWV by individual analysis of Cd^{2+}, Pb^{2+}, Cu^{2+}, and Hg^{2+}, respectively.

The enhanced electrochemical performance can be ascribed to three factors: (1) rGO could be used to prevent the aggregation of Co_3O_4 nanoribbons/NPs, resulting in fast migration of electrons; (2) PEI might prevent the aggregation of Co_3O_4 nanoribbons/NPs and provide more binding sites to bond with the target HMIs as they possess a lot of N functional groups; (3) the Co_3O_4 nanoribbons with active (110) and (220) planes retain the chemical sensitivity and adsorb HMIs. The approach developed in the present work provides a novel route for low-cost and comprehensive porous rGO·Co_3O_4·PEI with highly promising applications in heavy metal detection.

4. EXPERIMENTAL SECTION

4.1. Chemicals. All the chemicals used in this study were of analytical grade and used without further purification. Cobalt nitrate hexahydrate [$Co(NO_3)_2·6H_2O$, 99%] and sodium hydroxide (NaOH, 96%) were provided by Xilong Chemical Co., Ltd. Hydrochloric acid (HCl, 37%) was obtained from Beijing Chemical Works. Branched PEI (M_W = 600, 99%) was bought from Alfa Aesar Chemical Co. Ltd. (Tianjin, China). Lead nitrate [$Pb(NO_3)_2$], cadmium nitrate tetrahydrate [$Cd(NO_3)_2·4H_2O$], copper nitrate trihydrate [$Cu(NO_3)_2·3H_2O$], mercury nitrate [$Hg(NO_3)_2$], acetic acid, and sodium acetate were provided by Tianjin Chemical Works. EG of 300 mesh used in the preparation of rGO·PEI and rGO·Co_3O_4·PEI NCP was obtained from Qingdao Tianyuan Chemical Co., Ltd. Concentrated sulfuric acid (H_2SO_4, 98%) was purchased from Yaohua Chemical Reagent Co. Ltd. (Tianjin, China).

4.2. Synthesis of the rGO·Co_3O_4·PEI NCP. The thin-sheet-like structure of EG was attained by heating expandable graphite in a microwave oven. Graphite oxide was prepared by the Hummers method.[39] Then, 20 mL of PEI (2 g/L) and 80 mL of EG solution (0.03 g/L) were mixed with deionized (DI) water (100 mL) under magnetic stirring, the pH was adjusted (9.0 ± 0.2), and the solution was allowed to stand for 1 h; then it was sonicated for 0.5 h, and 20 mL of $Co(NO_3)_2$ solution (2 g/L) was added dropwise to the solution. During the mixing process, the pH of the solution was kept at 9.0 ± 0.2. The flow rate of air was maintained as 50 mL/min for 20 min. Then, the pH of the solution (12.0 ± 0.2) was balanced by the gradual addition of NaOH solution and the air flow was maintained for 2 h. After the completion of aeration, the solution was further sonicated for 0.5 h followed by pH adjustment (12 ± 0.2). Finally, the mixed precursor solution was placed for 24 h at room temperature (RT), the precipitate was filtered and washed with DI water; the pH was adjusted to about 7. The obtained precipitates were dispersed in DI water and transferred to a 100 mL Teflon-lined stainless steel autoclave. The hydrothermal method was done at 190 °C for 5 h. The obtained rGO·Co_3O_4·PEI NCP was named rGO·Co_3O_4·PEI. When the $Co(NO_3)_2$ solution concentration was 30 and 40 mL, the obtained NCPs were named rGO·Co_3O_4·PEI-1 and rGO·Co_3O_4·PEI-2, respectively.

4.3. Characterizations. The morphological and surface compositions for NCPs were studied by SEM (HITACHI S-4800), EDS, and TEM (JEOL-2100) analyses. X-ray powder diffraction (XRD; D/Max-IIIB-40 kV, Japan, Cu Kα radiation, λ = 1.5406 Å) analysis was used to define the crystalline

https://doi.org/10.1021/acsomega.1c05989
ACS Omega 2022, 7, 5870−5882

structure and the composition of the assembled composites. FTIR measurements (PerkinElmer spectrometer, KBr pellet technique) and Raman spectroscopy (Jobin Yvon HR 800 micro-Raman spectrometer) were also performed. The surface composition study was done by XPS(AXIS ULPRA DLD Shimadzu Corporation). The porous PEI-functionalized Co_3O_4/rGO NCPs were characterized by XPS using an Mg Kα X-ray source ($h\nu$ = 1.254 MeV) and a 120 mm arched electron energy analyzer, with an energy resolution of ∼0.8 eV. Thermogravimetric (TG) quantification was achieved with a Shimadzu TGA-50.

For electrochemical experiments, a traditional three-electrode system electrochemical workstation (Beijing Company CHI660D) was used. The Ag/AgCl electrode (no 218 ± 3 potential) purchased from the Shanghai Branch of the Inst. Eq. Company and platinum (Pt J110, with the snap width below 1 mm) made at Tianjin Ida Heng Sheng Tech. Dev. Co., Ltd. were used as the reference and auxiliary electrodes, respectively. SWV and DNPV electrochemical analyses were conducted to detect the four HMIs (Cd^{2+}, Pb^{2+}, Cu^{2+}, and Hg^{2+}). Both SWV and DNPV were performed with a three-electrode cell using a CHI660D electrochemical workstation.

The GCE coated with rGO·Co_3O_4·PEI was used as the working electrode for EIS, CV, MS measurements, and SWV experiments. The CV responses of rGO·Co_3O_4·PEI-modified electrodes were studied in $Fe(CN)_6^{3-/4-}$ (5 mM) solution comprising KCl (1 M) using the $Fe(CN)_6^{3-/4-}$ redox couple, and the pH was attuned to 5 ± 02 with acetate buffer solution (CH_3COOH/CH_3COONa). The EIS experiments were carried out between −0.2 and 0.6 V at RT with Ag/AgCl as the reference electrode and a Pt electrode as the counter electrode. EIS experiments were completed with an initial potential of 0.294 V in the frequency range of 1 Hz to 0.1 μHz.shikeying2008@163.com

■ ASSOCIATED CONTENT

Supporting Information

The Supporting Information is available free of charge at https://pubs.acs.org/doi/10.1021/acsomega.1c05989.

TEM images of rGO from expanded graphene and rGO·PEI NCP; TEM and HRTEM images of rGO·PEI NCP; TEM image and EDS spectrum of porous rGO·Co_3O_4·PEI NCP; TEM and HRTEM images of porous rGO·Co_3O_4·PEI-1 NCP; TEM images of rGO·Co_3O_4·PEI-1 and rGO·Co_3O_4·PEI-2 NCP; spinel structure of the Co_3O_4 nanoribbon crystal and surface atomic configuration of Co_3O_4; HRTEM images of {220}, {111}, and {110} planes; crystallographic planes and planar density in {111}, {110}, and {220} planes along with the arrangement of atoms; weight lost by VS heat flow; fitted impedance parameters of rGO·Co_3O_4·PEI NCPs; MS results and carrier densities of rGO·Co_3O_4·PEI NCP; individual analysis of rGO·Co_3O_4·PEI NCP; linearization equations, adj. R^2 response of rGO·Co_3O_4·PEI NCP-modified GCE and calibration curves for the simultaneous voltammetry investigation of Cd^{2+}, Pb^{2+}, Cu^{2+}, and Hg^{2+}; CV curves of GO, rGO, rGO·PEI, and rGO·Co_3O_4-modified electrode; EIS curves of GO, rGO, rGO·PEI, and rGO·Co_3O_4-modified electrode; SWV curves of rGO, rGO·PEI, and rGO·Co_3O_4 NCP; SWV analysis at 10 μM concentration and 5 μM concentration of the four HMIs; XPS full spectrum of the PEI-functionalized Co_3O_4/rGO NCP; Co 2p XPS spectrum of the PEI-functionalized Co_3O_4/rGO NCP; statistical calculation data of LOD for simultaneous sensing/detection of the four HMIs using the SWV voltammetry technique; statistical calculation data of LOD for simultaneous degradation of the four HMIs using the DNPV voltammetry technique; statistical calculation data of LOD for individual detection of the four HMIs using the SWV voltammetry technique; results of the porous rGO·Co_3O_4·PEI NCP used for the simultaneous and individual analyses of HMIs by using the SWV electrochemical method; comparison of the LOD (individual analysis via SWV and simultaneous analysis via SWV and DNPV); comparison of simultaneous analysis of HMIs via SWV and WHO; comparison of sensitivity; and comparison study of rGO·Co_3O_4·PEI NCP with previous work used for the sensing/detection of Cd^{2+}, Pb^{2+}, Cu^{2+}, and Hg^{2+} (PDF)

■ AUTHOR INFORMATION

Corresponding Author

Afrasiab Ur Rehman − *Department of Chemistry, Khushal Khan Khattak University, Karak, 27200 Karak, Khyber Pakhtunkhawa, Pakistan; Key Laboratory of Functional Inorganic Material Chemistry, Ministry of Education. School of Chemistry and Material Science, Heilongjiang University, Harbin 150080, P. R. China;* orcid.org/0000-0002-2217-7398; Phone: +923490574199; Email: dr.afrasiab@kkkuk.edu.pk

Authors

Muhammad Fayaz − *Department of Chemistry, Khushal Khan Khattak University, Karak, 27200 Karak, Khyber Pakhtunkhawa, Pakistan*

He Lv − *Key Laboratory of Functional Inorganic Material Chemistry, Ministry of Education. School of Chemistry and Material Science, Heilongjiang University, Harbin 150080, P. R. China*

Yang Liu − *Key Laboratory of Functional Inorganic Material Chemistry, Ministry of Education. School of Chemistry and Material Science, Heilongjiang University, Harbin 150080, P. R. China*

Jiawei Zhang − *Modern Experiment Center, Harbin Normal University, Harbin 150025, P. R. China*

Yang Wang − *Key Laboratory of Functional Inorganic Material Chemistry, Ministry of Education. School of Chemistry and Material Science, Heilongjiang University, Harbin 150080, P. R. China*

Lijuan Du − *Modern Experiment Center, Harbin Normal University, Harbin 150025, P. R. China*

Ruihong Wang − *Key Laboratory of Functional Inorganic Material Chemistry, Ministry of Education. School of Chemistry and Material Science, Heilongjiang University, Harbin 150080, P. R. China*

Keying Shi − *Key Laboratory of Functional Inorganic Material Chemistry, Ministry of Education. School of Chemistry and Material Science, Heilongjiang University, Harbin 150080, P. R. China;* orcid.org/0000-0002-9549-0190

Complete contact information is available at: https://pubs.acs.org/10.1021/acsomega.1c05989

https://doi.org/10.1021/acsomega.1c05989
ACS Omega 2022, 7, 5870−5882

Notes

The authors declare no competing financial interest.

■ ACKNOWLEDGMENTS

The present work relied on the Innovative Research Team (IRT1237) Program in Chinese universities, the National Natural Science Foundation of China (no. 2167010747), the Heilongjiang Provincial Education Department Scientific Research Fund (nos. 12521421, PEBM201502, and RC2012XK018005), and the Heilongjiang Province Innovation and Entrepreneurship Training Project for College Students (201610231042).

■ REFERENCES

(1) Battistel, D.; Baldi, F.; Marchetto, D.; Gallo, M.; Daniele, S. A Rapid Electrochemical Procedure for the Detection of Hg(0) Produced by Mercuric-Reductase: Application for Monitoring Hg-resistant Bacteria Activity. *Environ. Sci. Technol.* **2012**, *46*, 10675−10681.

(2) Gao, C.; Yu, X.-Y.; Xu, R.-X.; Liu, J.-H.; Huang, X.-J. AlOOH-Reduced Graphene Oxide Nanocomposites: One-Pot Hydrothermal Synthesis and Their Enhanced Electrochemical Activity for Heavy Metal Ions. *ACS Appl. Mater. Interfaces* **2012**, *4*, 4672−4682.

(3) Yao, X.-Z.; Guo, Z.; Yuan, Q.-H.; Liu, Z.-G.; Liu, J.-H.; Huang, X.-J. Exploiting Differential Electrochemical Stripping Behaviors of Fe_3O_4 Nanocrystals toward Heavy Metal Ions by Crystal Cutting. *ACS Appl. Mater. Interfaces* **2014**, *6*, 12203−12213.

(4) Qin, X.; Xu, A.; Wang, L.; Liu, L.; Chao, L.; He, F.; Tan, Y.; Chen, C.; Xie, Q. In situ microliter-droplet anodic stripping voltammetry of copper stained on the gold label after galvanic replacement reaction enlargement for ultrasensitive immunoassay of proteins. *Biosens. Bioelectron.* **2016**, *79*, 914−921.

(5) Wang, N.; Lin, M.; Dai, H.; Ma, H. Functionalized gold nanoparticles/reduced graphene oxide nanocomposites for ultrasensitive electrochemical sensing of mercury ions based on thymine-mercury-thymine structure. *Biosens. Bioelectron.* **2016**, *79*, 320−326.

(6) Aragay, G.; Pons, J.; Merkoçi, A. Recent Trends in Macro-, Micro-, and Nanomaterial-Based Tools and Strategies for Heavy-Metal Detection. *Chem. Rev.* **2011**, *111*, 3433−3458.

(7) Wang, B.; Luo, B.; Liang, M.; Wang, A.; Wang, J.; Fang, Y.; Chang, Y.; Zhi, L. Chemical amination of graphene oxides and their extraordinary properties in the detection of lead ions. *Nanoscale* **2011**, *3*, 5059−5066.

(8) Xu, X.; Duan, G.; Li, Y.; Liu, G.; Wang, J.; Zhang, H.; Dai, Z.; Cai, W. Fabrication of Gold Nanoparticles by Laser Ablation in Liquid and Their Application for Simultaneous Electrochemical Detection of Cd^{2+}, Pb^{2+}, Cu^{2+}, Hg^{2+}. *ACS Appl. Mater. Interfaces* **2014**, *6*, 65−71.

(9) Long, F.; Gao, C.; Shi, H. C.; He, M.; Zhu, A. N.; Klibanov, A. M.; Gu, A. Z. Reusable evanescent wave DNA biosensor for rapid, highly sensitive, and selective detection of mercury ions. *Biosens. Bioelectron.* **2011**, *26*, 4018−4023.

(10) Lin, M.; Cho, M.; Choe, W.-S.; Yoo, J.-B.; Lee, Y. Polypyrrole nanowire modified with Gly-Gly-His tripeptide for electrochemical detection of copper ion. *Biosens. Bioelectron.* **2010**, *26*, 940−945.

(11) Zhang, Z.; Ji, H.; Song, Y.; Zhang, S.; Wang, M.; Jia, C.; Tian, J.-Y.; He, L.; Zhang, X.; Liu, C.-S. Fe(III)-based Metal-Organic Framework-derived Core-shell Nanostructure: Sensitive Electrochemical Platform for High Trace Determination of Heavy Metal Ions. *Biosens. Bioelectron.* **2017**, *94*, 358−364.

(12) Sun, H.; Li, W.; Dong, Z.-Z.; Hu, C.; Leung, C.-H.; Ma, D.-L.; Ren, K. A suspending-droplet mode paper-based microfluidic platform for low-cost, rapid, and convenient detection of lead(II) ions in liquid solution. *Biosens. Bioelectron.* **2018**, *99*, 361−367.

(13) Zaib, M.; Athar, M. M.; Saeed, A.; Farooq, U. Electrochemical determination of inorganic mercury and arsenic-A review. *Biosens. Bioelectron.* **2015**, *74*, 859−908.

(14) Sun, Y.-F.; Wang, J.; Li, P.-H.; Yang, M.; Huang, X.-J. Highly sensitive electrochemical detection of Pb(II) based on excellent adsorption and surface Ni(II)/Ni(III) cycle of porous flower-like NiO/rGO nanocomposite. *Sens. Actuators, B* **2019**, *292*, 136−147.

(15) Han, S.; Zhou, X.; Tang, Y.; He, M.; Zhang, X.; Shi, H.; Xiang, Y. Practical, highly sensitive, and regenerable evanescent-wave biosensor for detection of Hg^{2+} and Pb^{2+} in water. *Biosens. Bioelectron.* **2016**, *80*, 265−272.

(16) Natile, M. M.; Glisenti, A. Study of Surface Reactivity of Cobalt Oxides: Interaction with Methanol. *Chem. Mater.* **2002**, *14*, 3090−3099.

(17) Qi, Y.; Zhang, H.; Du, N.; Zhai, C.; Yang, D. Synthesis of Co_3O_4@SnO_2@C core-shell nanorods with superior reversible lithium-ion storage. *RSC Adv.* **2012**, *2*, 9511−9516.

(18) Zhou, G.; Li, L.; Zhang, Q.; Li, N.; Li, F. Octahedral Co_3O_4 particles threaded by carbon nanotube arrays as integrated structure anodes for lithium ion batteries. *Phys. Chem. Chem. Phys.* **2013**, *15*, 5582−5587.

(19) Peng, L.; Feng, Y.; Bai, Y.; Qiu, H.-J.; Wang, Y. Designed synthesis of hollow Co_3O_4 nanoparticles encapsulated in a thin carbon nanosheet array for high and reversible lithium storage. *J. Mater. Chem. A* **2015**, *3*, 8825−8831.

(20) Yao, W. L.; Chen, J. Q.; Li, A. Y.; Chen, X. B. Novel Co_3O_4/Carbon Nanofiber Composite Electrode with High Li-Storage Capacity for Lithium Ion Batteries. *Adv. Mater. Res.* **2011**, *197−198*, 1113−1116.

(21) Zhou, W.; Vavro, J.; Nemes, N. M.; Fischer, J. E.; Borondics, F.; Kamarás, K.; Tanner, D. B. Charge transfer and Fermi level shift inp-doped single-walled carbon nanotubes. *Phys. Rev. B: Condens. Matter Mater. Phys.* **2005**, *71*, 205423.

(22) Xiao, J.; Chen, C.; Xi, J.; Xu, Y.; Xiao, F.; Wang, S.; Yang, S. Core-shell Co@Co_3O_4 nanoparticle-embedded bamboo-like nitrogen-doped carbon nanotubes (BNCNTs) as a highly active electrocatalyst for the oxygen reduction reaction. *Nanoscale* **2015**, *7*, 7056−7064.

(23) Kim, M. S.; Lim, E.; Kim, S.; Jo, C.; Chun, J.; Lee, J. General Synthesis of N-Doped Macroporous Graphene-Encapsulated Mesoporous Metal Oxides and Their Application as New Anode Materials for Sodium-Ion Hybrid Supercapacitors. *Adv. Funct. Mater.* **2017**, *27*, 1603921.

(24) Yang, Y.; Tian, C.; Sun, L.; Lü, R.; Zhou, W.; Shi, K.; Kan, K.; Wang, J.; Fu, H. Growth of small sized CeO_2 particles in the interlayers of expanded graphite for high-performance room temperature NOx gas sensors. *J. Mater. Chem. A* **2013**, *1*, 12742−12749.

(25) Xing, X.; Liu, R.; Liu, S.; Xiao, S.; Xu, Y.; Wang, C.; Wu, D. Surfactant-Assisted Hydrothermal Synthesis of Cobalt Oxide/Nitrogen-Doped Graphene Framework for Enhanced Anodic Performance in Lithium Ion Batteries. *Electrochim. Acta* **2016**, *194*, 310−316.

(26) Yang, Y.; Huang, J.; Zeng, J.; Xiong, J.; Zhao, J. Direct Electrophoretic Deposition of Binder-Free Co_3O_4/Graphene Sandwich-Like Hybrid Electrode as Remarkable Lithium Ion Battery Anode. *ACS Appl. Mater. Interfaces* **2017**, *9*, 32801−32811.

(27) Wang, T.; Wang, J.; Yang, Y.; Su, P.; Yang, Y. Co_3O_4/Reduced Graphene Oxide Nanocomposites as Effective Phosphotriesterase Mimetics for Degradation and Detection of Paraoxon. *Ind. Eng. Chem. Res.* **2017**, *56*, 9762−9769.

(28) Wang, L.; Zheng, Y.; Wang, X.; Chen, S.; Xu, F.; Zuo, L.; Wu, J.; Sun, L.; Li, Z.; Hou, H.; Song, Y. Nitrogen-Doped Porous Carbon/Co_3O_4 Nanocomposites as Anode Materials for Lithium-Ion Batteries. *ACS Appl. Mater. Interfaces* **2014**, *6*, 7117−7125.

(29) Wang, S. X.; Sun, L. X.; Tan, Z. C.; Xu, F.; Li, Y. S. Synthesis, characterization and thermal analysis of polyaniline (PANI)/Co_3O_4 composites. *J. Therm. Anal. Calorim.* **2007**, *89*, 609−612.

(30) Poizot, P.; Laruelle, S.; Grugeon, S.; Dupont, L.; Tarascon, J.-M. Nano-sized transition-metal oxides as negative-electrode materials for lithium-ion batteries. *Nature* **2000**, *407*, 496−499.

(31) Yang, X.; Fan, K.; Zhu, Y.; Shen, J.; Jiang, X.; Zhao, P.; Li, C. Tailored graphene-encapsulated mesoporous Co_3O_4 composite microspheres for high-performance lithium ion batteries. *J. Mater. Chem.* **2012**, *22*, 17278−17283.

https://doi.org/10.1021/acsomega.1c05989
ACS Omega 2022, 7, 5870−5882

(32) Ezoddin, M.; Shemirani, F.; Abdi, K.; Saghezchi, M. K.; Jamali, M. R. Application of modified nano-alumina as a solid phase extraction sorbent for the preconcentration of Cd and Pb in water and herbal samples prior to flame atomic absorption spectrometry determination. *J. Hazard. Mater.* **2010**, *178*, 900−905.
(33) Zhang, L. H.; Shi, Y.; Wang, Y.; Shiju, N. R. Nanocarbon Catalysts: Recent Understanding Regarding the Active Sites. *Adv. Sci.* **2020**, *7*, 1902126.
(34) Yavuz, E.; Tokalıoğlu, Ş.; Şahan, H.; Patat, Ş. Ultralayered Co_3O_4 as a new adsorbent for preconcentration of Pb(II) from water, food, sediment and tobacco samples. *Talanta* **2013**, *115*, 724−729.
(35) Singh, S. K.; Dhavale, V. M.; Kurungot, S. Low Surface Energy Plane Exposed Co_3O_4 Nanocubes Supported on Nitrogen-Doped Graphene as an Electrocatalyst for Efficient Water Oxidation. *ACS Appl. Mater. Interfaces* **2015**, *7*, 442−451.
(36) Yu, X.-Y.; Meng, Q.-Q.; Luo, T.; Jia, Y.; Sun, B.; Li, Q.-X.; Liu, J.-H.; Huang, X.-J. Facet-dependent electrochemical properties of Co_3O_4 nanocrystals toward heavy metal ions. *Sci. Rep.* **2013**, *3*, 2886.
(37) Xie, X.; Li, Y.; Liu, Z.-Q.; Haruta, M.; Shen, W. Low-temperature oxidation of CO catalysed by Co_3O_4 nanorods. *Nature* **2009**, *458*, 746−749.
(38) Petitto, S. C.; Marsh, E. M.; Carson, G. A.; Langell, M. A. Cobalt oxide surface chemistry: The interaction of CoO(1 0 0), Co_3O_4(1 1 0) and Co_3O_4(1 1 1) with oxygen and water. *J. Mol. Catal. A* **2008**, *281*, 49−58.
(39) Alam, S. N.; Sharma, N.; Kumar, L. Synthesis of Graphene Oxide (GO) by Modified Hummers Method and Its Thermal Reduction to Obtain Reduced Graphene Oxide (rGO)*. *Graphene* **2017**, *6*, 1−18.
(40) Omata, K.; Takada, T.; Kasahara, S.; Yamada, M. Active site of substituted cobalt spinel oxide for selective oxidation of COH_2. Part II. *Appl. Catal., A* **1996**, *146*, 255−267.
(41) Beaufils, J. P.; Barbaux, Y. Study of adsorption on powders by surface differential diffraction measurements. Argon on Co_3O_4. *Appl. Cryst.* **1982**, *15*, 301−307.
(42) Zhou, L.; Cao, S.; Zhang, L.; Xiang, G.; Wang, J.; Zeng, X.; Chen, J. Facet effect of Co_3O_4 nanocatalysts on the catalytic decomposition of ammonium perchlorate. *J. Hazard. Mater.* **2020**, *392*, 122358.
(43) Ziókowski, J.; Barbaux, Y. Identification of sites active in oxidation of butene-1 to butadiene and CO_2 on CO_3O_4 in terms of the crystallochemical model of solid surfaces. *J. Mol. Catal.* **1991**, *67*, 199−215.
(44) Zheng, Y.; Gao, R.; Zheng, L.; Sun, L.; Hu, Z.; Liu, X. Ultrathin Co_3O_4 Nanosheets with Edge-Enriched {111} Planes as Efficient Catalysts for Lithium−Oxygen Batteries. *ACS Catal.* **2019**, *9*, 3773−3782.
(45) Sun, L.; Deng, Q.; Li, Y.; Mi, H.; Wang, S.; Deng, L.; Ren, X.; Zhang, P. CoO-Co_3O_4 heterostructure nanoribbon/RGO sandwich-like composites as anode materials for high performance lithium-ion batteries. *Electrochim. Acta* **2017**, *241*, 252−260.
(46) Cai, D.; Huang, H.; Wang, D.; Liu, B.; Wang, L.; Liu, Y.; Li, Q.; Wang, T. High-Performance Supercapacitor Electrode Based on the Unique ZnO@Co_3O_4 Core/Shell Heterostructures on Nickel Foam. *ACS Appl. Mater. Interfaces* **2014**, *6*, 15905−15912.
(47) Zhou, S.; Ye, Z.; Hu, S.; Hao, C.; Wang, X.; Huang, C.; Wu, F. Designed formation of Co_3O_4/$ZnCo_2O_4$/CuO hollow polyhedral nanocages derived from zeolitic imidazolate framework-67 for high-performance supercapacitors. *Nanoscale* **2018**, *10*, 15771−15781.
(48) Fan, S.; Zhao, M.; Ding, L.; Li, H.; Chen, S. Preparation of Co_3O_4/crumpled graphene microsphere as peroxidase mimetic for colorimetric assay of ascorbic acid. *Biosens. Bioelectron.* **2017**, *89*, 846−852.
(49) Wu, Z.-S.; Ren, W.; Wen, L.; Gao, L.; Zhao, J.; Chen, Z.; Zhou, G.; Li, F.; Cheng, H.-M. Graphene Anchored with Co_3O_4 Nanoparticles as Anode of Lithium Ion Batteries with Enhanced Reversible Capacity and Cyclic Performance. *ACS Nano* **2010**, *4*, 3187−3194.
(50) Zhu, Z.; Lu, G.; Zhang, Z.; Guo, Y.; Guo, Y.; Wang, Y. Highly Active and Stable Co_3O_4/ZSM-5 Catalyst for Propane Oxidation: Effect of the Preparation Method. *ACS Catal.* **2013**, *3*, 1154−1164.
(51) Dong, X.-C.; Xu, H.; Wang, X.-W.; Huang, Y.-X.; Chan-Park, M. B.; Zhang, H.; Wang, L.-H.; Huang, W.; Chen, P. 3D Graphene-Cobalt Oxide Electrode for High-Performance Supercapacitor and Enzymeless Glucose Detection. *ACS Nano* **2012**, *6*, 3206−3213.
(52) Chen, Y.; Lu, Z.; Zhou, L.; Mai, Y.-W.; Huang, H. Triple-coaxial electrospun amorphous carbon nanotubes with hollow graphitic carbon nanospheres for high-performance Li ion batteries. *Energy Environ. Sci.* **2012**, *5*, 7898−7902.
(53) Li, Z. Q.; Lu, C. J.; Xia, Z. P.; Zhou, Y.; Luo, Z. X-ray diffraction patterns of graphite and turbostratic carbon. *Carbon* **2007**, *45*, 1686−1695.
(54) Huang, R.; Li, Y.; Song, Y.; Wang, L. Facial preparation of N-doped carbon foam supporting Co_3O_4 nanorod arrays as free-standing lithium-ion batteries anode. *J. Alloys Compd.* **2020**, *818*, 152839.
(55) Lai, L.; Zhu, J.; Li, Z.; Yu, D. Y. W.; Jiang, S.; Cai, X.; Yan, Q.; Lam, Y. M.; Shen, Z.; Lin, J. Co_3O_4/nitrogen modified graphene electrode as Li-ion battery anode with high reversible capacity and improved initial cycle performance. *Nano Energy* **2014**, *3*, 134−143.
(56) Meng, X.; Zhong, Y.; Sun, Y.; Banis, M. N.; Li, R.; Sun, X. Nitrogen-doped carbon nanotubes coated by atomic layer deposited SnO_2 with controlled morphology and phase. *Carbon* **2011**, *49*, 1133−1144.
(57) Ma, L.; Zhou, H.; Shen, X.; Chen, Q.; Zhu, G.; Ji, Z. Facile synthesis of Co_3O_4 porous nanosheets/reduced graphene oxide composites and their excellent supercapacitor performance. *RSC Adv.* **2014**, *4*, 53180−53187.
(58) Zhu, X.; Ning, G.; Ma, X.; Fan, Z.; Xu, C.; Gao, J.; Xu, C.; Wei, F. High density Co_3O_4 nanoparticles confined in a porous graphene nanomesh network driven by an electrochemical process: ultra-high capacity and rate performance for lithium ion batteries. *J. Mater. Chem. A* **2013**, *1*, 14023−14030.
(59) Soo, H. S.; Agiral, A.; Bachmeier, A.; Frei, H. Visible Light-Induced Hole Injection into Rectifying Molecular Wires Anchored on Co_3O_4 and SiO_2 Nanoparticles. *J. Am. Chem. Soc.* **2012**, *134*, 17104−17116.
(60) Shi, P.; Su, R.; Wan, F.; Zhu, M.; Li, D.; Xu, S. Co_3O_4 nanocrystals on graphene oxide as a synergistic catalyst for degradation of Orange II in water by advanced oxidation technology based on sulfate radicals. *Appl. Catal., B* **2012**, *123−124*, 265−272.
(61) Zhu, J.; Sharma, Y. K.; Zeng, Z.; Zhang, X.; Srinivasan, M.; Mhaisalkar, S.; Zhang, H.; Hng, H. H.; Yan, Q. Cobalt Oxide Nanowall Arrays on Reduced Graphene Oxide Sheets with Controlled Phase, Grain Size, and Porosity for Li-Ion Battery Electrodes. *J. Phys. Chem. C* **2011**, *115*, 8400−8406.
(62) Zhuo, L.; Wu, Y.; Ming, J.; Wang, L.; Yu, Y.; Zhang, X.; Zhao, F. Facile synthesis of a Co_3O_4-carbon nanotube composite and its superior performance as an anode material for Li-ion batteries. *J. Mater. Chem. A* **2013**, *1*, 1141−1147.
(63) Shao, J.; Zhou, H.; Zhu, M.; Feng, J.; Yuan, A. Facile synthesis of metal-organic framework-derived Co_3O_4 with different morphologies coated graphene foam as integrated anodes for lithium-ion batteries. *J. Alloys Compd.* **2018**, *768*, 1049−1057.
(64) Dai, J.; Song, M.; Wang, M.; Li, P.; Zhang, C.; Shen, Y.; Xie, A. Freeze-drying growth of Co_3O_4/N-doped reduced graphene oxide nanocomposite as excellent anode material for lithium-ion batteries. *Ceram. Int.* **2016**, *42*, 2410−2415.
(65) Casella, I. G.; Gatta, M. Study of the electrochemical deposition and properties of cobalt oxide species in citrate alkaline solutions. *J. Electroanal. Chem.* **2002**, *534*, 31−38.
(66) Ben-Bassat, A. H. I.; Azrad, A. Intermetallic compounds formed in mixed (complex) amalgams-I. The systems: copper-mercury, zinc-mercury and copper-zinc-mercury. *Electrochim. Acta* **1978**, *23*, 63−69.
(67) Gumpu, M. B.; Sethuraman, S.; Krishnan, U. M.; Rayappan, J. B. B. A review on detection of heavy metal ions in water - An electrochemical approach. *Sens. Actuators, B* **2015**, *213*, 515−533.

https://doi.org/10.1021/acsomega.1c05989
ACS Omega 2022, 7, 5870−5882

(68) Tibbetts, D. F.; Davis, J.; Compton, R. G. Sonoelectroanalytical detection of lead at a bare copper electrode. *Fresenius. J. Anal. Chem.* **2000**, *368*, 412−414.
(69) Wei, Y.; Gao, C.; Meng, F.-L.; Li, H.-H.; Wang, L.; Liu, J.-H.; Huang, X.-J. SnO_2/Reduced Graphene Oxide Nanocomposite for the Simultaneous Electrochemical Detection of Cadmium(II), Lead(II), Copper(II), and Mercury(II): An Interesting Favorable Mutual Interference. *J. Phys. Chem. C* **2012**, *116*, 1034−1041.

https://doi.org/10.1021/acsomega.1c05989
ACS Omega 2022, 7, 5870−5882